Article

Dark brown carbon from wildfires: a potent snow radiative forcing agent?

Check for updates

Ganesh S. Chelluboyina [ID], Taveen S. Kapoor [ID] & Rajan K. Chakrabarty [ID] ✉

Deposition of wildfire smoke on snow contributes to its darkening and accelerated snowmelt. Recent field studies have identified dark brown carbon (d-BrC) to contribute 50–75% of shortwave absorption in wildfire smoke. d-BrC is a distinct class of water-insoluble, light-absorbing organic carbon that co-exists in abundance with black carbon (BC) in snow across the world. However, the importance of d-BrC as a snow warming agent relative to BC remains unexplored. We address this gap using aerosol-snow radiative transfer calculations on datasets from laboratory and field measurement. We show d-BrC increases the annual mean snow radiative forcing between 0.6 and 17.9 W m^{-2}, corresponding to different wildfire smoke deposition scenarios. This is a 1.6 to 2.1-fold enhancement when compared with BC-only deposition on snow. This study suggests d-BrC is an important contributor to snowmelt in midlatitude glaciers, where ~40% of the world's glacier surface area resides.

Wildfire smoke plumes contain light-absorbing carbonaceous aerosols, which have long been linked to increased snowmelt through dry and wet deposition processes[1,2]. These aerosols darken snow surfaces reducing their reflectance (albedo), and accelerate snowmelt by absorbing additional solar energy[3,4]. Pristine snow, by contrast, is one of the most reflective of naturally occurring surfaces, with reflectance approaching 100% in the ultraviolet (UV) and near-visible wavelengths of the electromagnetic spectrum[5]. Particulate deposition, particularly of short wavelength absorbing aerosols, cause a relatively larger drop in albedo at those wavelengths compared to longer wavelengths[6]. Apart from light-absorbing aerosols, enhanced dust emissions may also occur in the aftermath of wildfires[7], which can decrease snow albedo. Additionally, charred and burned woody debris from wildfires have been observed to decrease the snow albedo in the immediate neighborhood of burned forests by half[8]. Snow darkening also occurs by other means not linked to wildfires, such as volcanic ash[9], mineral dust deposition[10], and snow algae growth[11,12]. However, wildfire-linked snow darkening is of particular concern since the numbers and areas of wildfires have trended sharply upwards in recent decades[13]. Moreover, wildfire smoke plumes may be transported thousands of kilometers from their source region and across continents, presenting a global environmental challenge[14].

The snow darkening effect on a glacier due to a single wildfire event may last years afterwards, even without further particle deposition[15]. In-situ field measurements have observed the darkening effect due to carbonaceous aerosols of wildfire origin in action[16–19]. A forest fire in the Olympic Peninsula of Washington state in the USA elevated the concentrations of black carbon on an alpine glacier subsequently enhancing its melt[17].

Globally, carbonaceous aerosols, some of which are transported from distant fires, have been found to be important snow surface radiative forcers: on Andean glaciers[16], the Tibetan plateau[18], the Arctic[19], and Antarctica[20]. In the Indian Himalayas, aerosol snow darkening has led to earlier snowmelt by 20 days and an increase in the temperature of both snow and air[21]. Several of these snowpacks are located in the mountain ranges of the mid-latitudes, where wildfire smoke is an increasingly common occurrence as a consequence of lengthening fire seasons[22] and decreasing precipitation[23]. Mid-latitude snowpacks are particularly vulnerable to deposition of pollution particles of urban and vehicular origin as well[24]. Harboring 99.95% of the world's population, the low and midlatitudes contain nearly 40% of the surface area of the world's glaciers, which directly sustain a quarter of global humanity[25,26].

Biomass burning, from sources including peatland fires and wildfires, emit organic carbon (OC) and black carbon (BC) aerosols. BC particles are the strongest light absorbing particles in biomass burning smoke[27]. OC dominates by mass, constituting >95% of this smoke[28], however, the extent of absorption due to these aerosols is highly uncertain. Light-absorbing OC, commonly known as brown carbon (BrC), absorbs predominantly in the near ultraviolet (200–400 nm) and the visible and near-infrared (VNIR) regions (400–1000 nm) of the electromagnetic spectrum. BrC light absorption strength spans several orders of magnitude (imaginary refractive index, k_{550} ranges from 10^{-3} to 0.25). Saleh et al.[29] reported the brown-black continuum, which arranges BrC light-absorption magnitudes along a continuum between weakly absorbing BrC and strongly absorbing BC. Particles in the upper range (k_{550} from 0.1 to 0.25) of BrC light absorption

Center for Aerosol Science and Engineering, Department of Energy, Environmental and Chemical Engineering, Washington University in St. Louis, St. Louis, MO, USA. ✉e-mail: chakrabarty@wustl.edu

(Fig. 1a), identified as dark brown carbon (d-BrC), are refractory and water insoluble, with BC-like properties, and are often co-emitted with BC in biomass burning[30]. Although refractory, d-BrC, which has been observed in both laboratory studies and in the field[29,30], shows a differential single-particle soot photometer (SP2) signal to BC[31]. In the 2019 NOAA/NASA Fire Influence on Regional to Global Environments and Air Quality (FIREX-AQ) field campaign, d-BrC was found to be four times more abundant than BC in wildfire smoke[30]. However, unlike BC, gaps remain in the understanding of d-BrC interactions with snow[32,33]. While the radiative effects of some types of BrC classified under water-soluble organic carbon (WSOC) have been well studied[34], they are much less light absorbing than the insoluble d-BrC. Meanwhile, field studies on Himalayan–Tibetan Plateau glaciers[35] and the Greenland ice sheet[36] have observed water-insoluble organic carbon (WIOC)/BC ratios exceeding 10 (Fig. 1b), revealing the significant presence of WIOC which encompasses the optical category of d-BrC. Moreover, water-insoluble particles like d-BrC are less likely to be scavenged and thus remain at the surface, where they have the largest impact on albedo[37].

Deposition experiments have also been performed to investigate the spectral albedo of snow laden with light-absorbing particles (LAPs) in controlled settings. Beres et al.[38] artificially deposited biomass burning particles from controlled combustion onto a snow field and isolated the radiative forcing (RF) due to BrC. Hadley and Kirchstetter[3] generated artificial snow to estimate radiative forcing and the changes in albedo in response to experimental BC aerosol deposition. In tandem with these measurements, spectral albedo was simulated using the SNow, ICe, and Aerosol Radiative (SNICAR) model, a two-stream radiative transfer model that can incorporate a suite of LAPs, including black and brown carbon aerosols[39,40]. SNICAR-based spectral albedo simulations have been employed in such studies to compare with experimental results and to estimate the LAP-induced radiative forcing. SNICAR has also been used as a stand-alone tool for modeling and meta-analysis[40–42].

Although BC radiative forcing has been well-quantified globally[43], the importance of BC as a radiative forcer in snow has been declining as BC deposition on snow peaked in the 1980s owing to the success of fossil fuel emission regulations[44–46]. Previous studies have attempted to determine aerosol snow radiative forcing, but only a few consider the influence of OC or attribute any of the radiative forcing to OC[17,47]. They also don't consider d-BrC, which have been recently shown to dominate aerosol absorption in wildfire emissions[30]. When measured albedo perturbation from clean snow is directly translated to radiative forcing in snow, the lack of rigorous partitioning among aerosols may lead to misattribution of what contributes to

the snow warming. This may lead to unseen biases when predicting radiative forcing where observational data is not available. Here we address this gap through an aerosol-snow coupled modeling approach by running albedo simulation experiments inclusive of d-BrC, which we represent through laboratory and field-observed optical datasets.

Results

Albedo sensitivity to d-BrC parameters and snow age

d-BrC particles exhibit a wide range of absorption which can be characterized by their imaginary part of the complex refractive index at 550 nm (k_{550}). Their k_{550} values range from 0.1 to 0.25 in d-BrC observed under variable laboratory combustion conditions[29] (brown-black continuum), while those observed in a real-world wildfire[30] show an intermediate value of 0.19. The spectral refractive index constitutes a d-BrC intensive property, upon which we applied Mie theory on a lognormal size distribution to determine the d-BrC ensemble optical properties: single scatter albedo, asymmetry parameter, and mass extinction coefficient.

We also consider the part-per-billion (ppb) mixing ratio by mass of d-BrC particles in snow, here forth referred to as "d-BrC concentration" (units of ppb, $ng\,g^{-1}$, or $\mu g\,L^{-1}$), as a tunable extensive property. Since d-BrC is at least four times as abundant by number and mass concentration as BC in real-world wildfire smoke[30], we consider d-BrC concentrations up to an order of magnitude higher than the typical BC range in snow. Although d-BrC has not been directly measured in snow yet, from the presence of large amounts of WIOC observed in snow[35], and from the evidence that d-BrC is co-emitted with BC[30], it can be inferred that d-BrC is present in snow along with BC. Data from field studies across the globe show that the observed concentrations of BC in snow can range from less than 1 ppb to more than 10^3 ppb[3,43]. In this work, we considered three orders of magnitude of BC concentration spanning from 10^1 to 10^3 ppb; therefore the corresponding maximum d-BrC concentrations spanned from 10^2 to 10^4 ppb. Each order of magnitude in this range, from low to high, may be considered to broadly represent low, medium, and high pollution in snow. Apart from the LAP optical properties and concentrations, snow microphysical properties including grain size, shape, and density influence the albedo. In this study we particularly consider grain size, since increasing grain size is correlated with decreasing albedo across all wavelengths[48]. Snow grain size of 100 μm is selected to represent freshly fallen, fine-grain ("fresh") snow and 1000 μm is selected to represent snow that has experienced grain growth ("aged")[39]. The term aging in this context thus refers exclusively to snow aging by grain growth, and not aerosol aging since both BC and d-BrC are inert, insoluble, and resist photobleaching[30]. Snow grain growth naturally occurs due to the
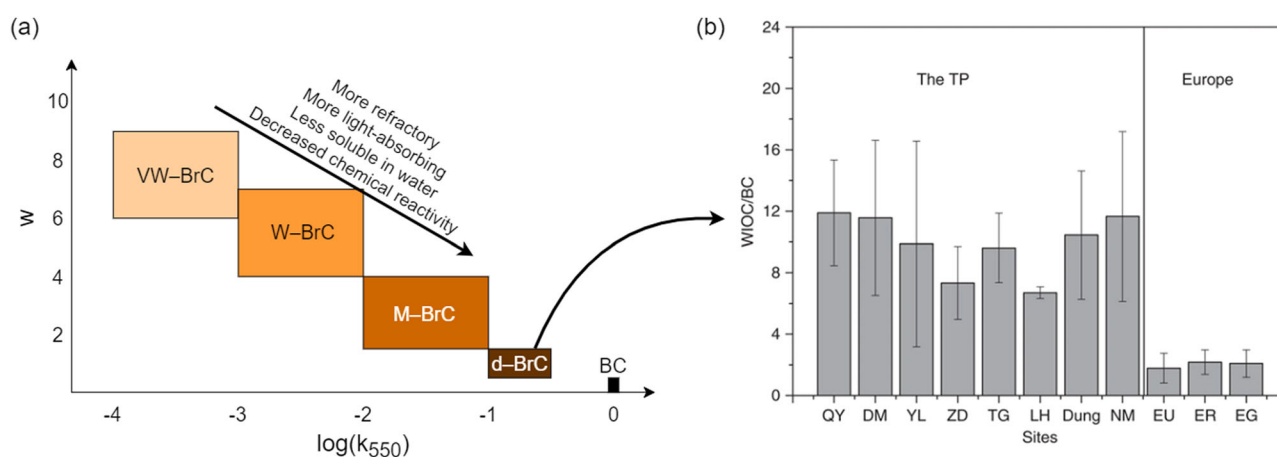

Fig. 1 | d-BrC optical and physicochemical properties in the atmosphere and its abundance relative to BC in snow. a The brown-black continuum of carbonaceous aerosols depicting the presence of a strongly absorbing fraction, d-BrC, which has a large imaginary refractive index at 550 nm k_{550} and low wavelength dependence w of spectral imaginary refractive index. This d-BrC is inert, refractory, resistant to

photobleaching, and insoluble in water[65]. Adapted from Saleh, R. Curr. Pollut. Rep. 6, 90–104 (2020). **b** Water-insoluble organic carbon (WIOC)/BC ratios observed in midlatitude Tibetan Plateau (TP) glaciers[35]. Reprinted from Li, C. et al. Nat. Commun. 7:12574 (2016). Distributed under a Creative Commons Attribution 4.0 License (CC BY 4.0) http://creativecommons.org/licenses/by/4.0/.

diurnal melt-freeze cycle[49], but is accelerated by the presence of heat-trapping particles in a positive feedback known as the "grain-size feedback"[4].

Taken together, the d-BrC ensemble optical properties, d-BrC concentration in snow, and the snow grain size are the three key tunable parameters used as inputs in the radiative transfer simulations of SNICAR, yielding spectral albedos. Figure 2, showing the combined spectral albedo results, depicts the complex interplay of these three parameters. Although the spectral albedos are most sensitive to snow aging, sensitivity to d-BrC k_{550} grows considerably in response to higher aerosol concentration and snow age.

The spectral albedo of 'No LAP Snow' is the baseline from which the LAP perturbs the spectral albedo. Note that the 'No LAP Snow' albedos differ for fresh snow (broadband albedo 0.97) versus aged snow (broadband albedo 0.91). While carbonaceous LAPs predominantly absorb at shorter wavelengths, snow grains moderately absorb at longer wavelengths[50]. Snow aging accentuates this infrared absorption trend because incident photons are more likely to be absorbed by snow with larger grains than smaller grains[48]. The contribution of a particular wavelength to the instantaneous radiative forcing (IRF) is proportional to the magnitude of this downward perturbation and the fraction of surface irradiance (height of the blue profile in the secondary axis plots of Fig. 2). From a cursory examination of Fig. 2, it is evident that shorter visible wavelengths are expected to contribute greater than longer wavelengths to the IRF. This follows from the nature of d-BrC's absorption which increases in magnitude with decreasing wavelength, as well as the spectral irradiance magnitude which is higher for shorter visible wavelengths. At 1000 nm, negligible perturbation is observed in all cases because of the dominance of snow absorption in the infrared wavelengths.

Snow aging and increasing d-BrC particle concentration (d-BrC mass mixing ratio in snow) both magnify albedo reductions in the near-UV-visible wavelengths. Furthermore, snow aging and increasing d-BrC particle concentration accentuate the spectral albedo spread due to variation in the d-BrC k_{550}, which is virtually negligible in the top left panel of Fig. 2. The spectral albedos tend to converge towards the UV wavelengths, due to a convergence of the d-BrC single-scattering albedo (SSA) in that wavelength region. The spectral albedos from each case are used to calculate the broadband albedos (Fig. S5), which are used in the radiative forcing calculations.

Comparative analysis of BC and d-BrC forcing

Radiative forcing of a species in snow refers to the amount of additional solar radiation (W m^{-2}) absorbed by the snow due to the presence of that species. Radiative forcing, both instantaneous and averaged over specific intervals of time, was estimated from the albedos of snow with and without LAPs. IRF was calculated first from broadband albedos, which are a function of solar zenith angle (SZA), snow grain size (d), k_{550}, and the LAP concentration, [LAP], according to Eq. 1:

$$IRF = \left[\bar{\alpha}_{no\,LAP}(SZA, d) - \bar{\alpha}_{LAP}(SZA, d, k_{550}, [LAP])\right] \cdot F_{bb}(SZA) \cdot f_{VNIR}$$

(1)

where $\bar{\alpha}_{no\,LAP}$ is the broadband albedo of snow with no LAP, $\bar{\alpha}_{LAP}$ is the broadband albedo of snow laden with LAP, F_{bb} is the surface broadband irradiance in W m^{-2} and f_{VNIR} is the fraction of the irradiance in the 400–1000 nm band, calculated to be 0.69. Mid-latitude profile of the surface irradiance was used[39]. We selected Mount Olympus (47.8152 °N, 123.7047 °W), in the U.S. Pacific Northwest, as the site for our radiative forcing analyses to be representative of mid-latitude mountain locations with snow cover in proximity to forest fires. Kaspari et al.[17] determined the black carbon content of snowpack here through an SP2 measuring the incandescence of re-aerosolized snow meltwater, following a major wildfire aerosol deposition event at Mt. Olympus. While they reported between 17 and 140 ppb of BC in ice cores extracted from the site, no measurements of d-BrC or WIOC were made.

The IRFs were determined at every half hour beginning at midnight each day (Fig. S7b). These half hour IRFs were averaged over 24-h intervals to give daily mean radiative forcing. Figure 3 shows the daily mean RF over a full year, calculated for three concentrations of BC and d-BrC (at its refractive index bounds) in aged snow. The seasonal variation of the radiative forcing is apparent, with the forcing peaking at the Northern Hemisphere summer solstice while minima occur at the winter solstice. This is because the solar irradiance is higher for smaller zenith angles, which occurs more frequently in the summer. Higher incident energy flux on snow during the summer allows for more heat to be trapped by LAPs. This

Fig. 2 | Spectral snow albedo sensitivity to d-BrC optical properties, d-BrC concentration in snow, and snow aging due to grain growth. The spectral albedos of snow at a 60° solar zenith angle in response to different d-BrC mixing scenarios are depicted. Spectral albedos of snow with no LAPs present are denoted by the dashed red line, while the spectral albedos of snow with d-BrC present are in brown. The secondary axis shows the solar irradiance profile, in blue, to emphasize overlap between peak irradiance wavelengths and region of relatively larger spectral albedo perturbation. d-BrC concentration increases in steps of an order of magnitude from the left-most panels to the right. The top row represents fresh snow (grain size 100 μm) and the bottom row represents aged snow (grain size 1000 μm). The various shades of brown represent varying imaginary part of the refractive index at 550 nm (k_{550}), with the darker lines representing more absorbing d-BrC.
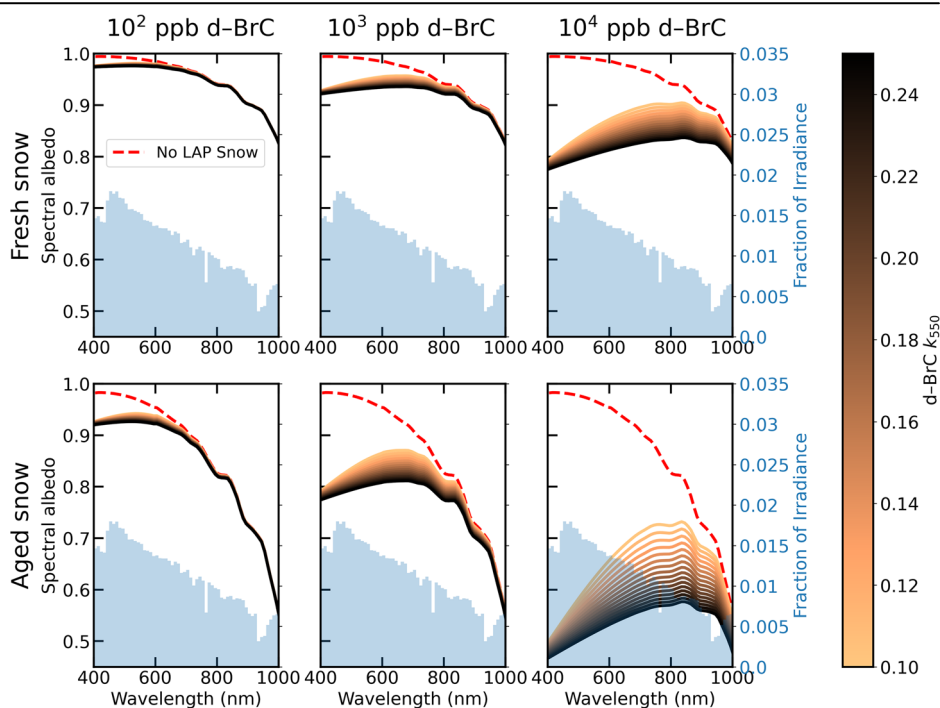
incident flux can go up to several hundred W m^{-2} during a summer midday leading to a high instantaneous RF. However, longer averaging durations reduce the average snow RF. For simplicity, LAP concentrations are considered temporally invariant, although wildfire frequency may vary seasonally. In all cases, forcing maxima is nearly an order of magnitude greater than corresponding forcing minima. Another key observation is that d-BrC creates less forcing than a similar concentration of BC, but greater forcing than BC of concentration an order of magnitude lower. This nontrivial forcing contribution may be important when considering biomass burning events where the d-BrC mass fractions dominate that of BC. Similar trends are observed in LAP-containing fresh snow, but with lower radiative forcing compared to the LAP-containing aged snow shown in Fig. 3. The seasonal variation of the daily mean RF plot (Fig. 3) is characteristic to the mid-latitudes of the northern hemisphere. In the southern hemisphere, this

variation would be inverted, while at higher latitudes the amplitude between the summer and winter solstices would be greater.

The daily mean RF predicted in Fig. 3 is comparable to the range reported in other studies in midlatitude mountains. Through satellite remote sensing, the daily mean RF on a mid-May day in the San Juan Mountains, Colorado[51] was calculated to be in the range 36–86 W m^{-2}. Based on field observations at Mt Olympus, Washington during a late-August week, the daily mean RF before a wildfire aerosol deposition event was 37–53 W m^{-2} while following the deposition it was 112–148 W m^{-2}.

We further plot the annual-mean radiative forcing due to particles spanning the full spectrum of k_{550} from 0.1 to 0.79, encompassing laboratory[29] and observed[30] d-BrC, and BC[52] (Fig. S8). Note the increasing trend of radiative forcing with increasing absorption power (higher k_{550}) of the LAP, increasing LAP concentration in snow, and increasing age of the snow. As mentioned previously, the presence of LAPs causes the grain-size feedback, whereby an initial albedo reduction heats up the snow causing grain growth, which begets further albedo reduction[4]. Therefore, in this study we primarily present results related to aged snow.

The concentrations of d-BrC emitted from wildfires are four[30] to ten times[35] that of BC. To account for this, abundance-weighted annual mean radiative forcing due to BC and d-BrC are calculated (Fig. S9). For each concentration of BC, the annual mean RF of d-BrC for a greater abundance, by a factor of between 4 and 10, was estimated. To ensure observational constraining, from here onwards all simulation experiments involving d-BrC are based on field-measured d-BrC optical properties ($k_{550} = 0.19$) rather than the brown-black continuum (k_{550} 0.1 to 0.25)[30]. The results show that for the observed d-BrC:BC abundance ratio of four[30], the d-BrC annual mean RF is between 22% and 46% greater than the co-emitted BC RF (corresponding to 10^3 ppb and 10 ppb of BC respectively). For an abundance ratio of 10, these are even larger, ranging from 83% to 187% higher than the co-emitted BC-only RF. This percentage decreases with increasing BC concentration as additional particles are less effective at reducing the albedo when particles are already present in the snow.
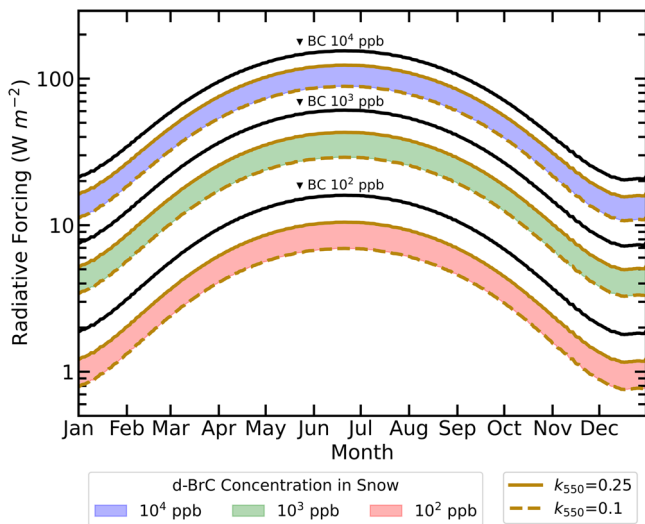
Combined analysis of BC and d-BrC forcing

As Fig. S9 demonstrates, when the species' relative abundances are factored in to determine abundance-weighted RFs, d-BrC emerges as a stronger radiative forcer in snow than BC, even though at the particle level BC is the stronger absorber. Therefore, we calculated the RF due to both species
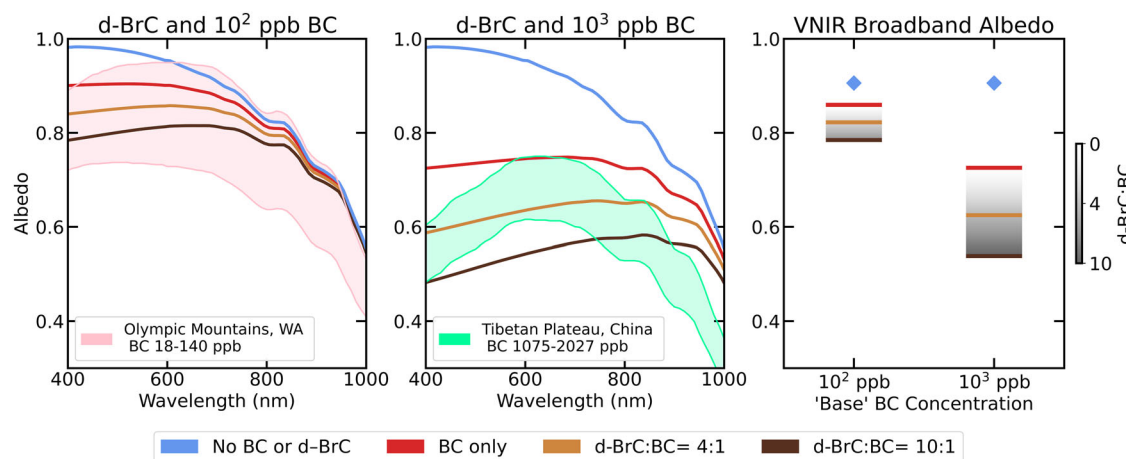

Fig. 3 | Daily mean radiative forcing over the span of a year. Simulation-derived daily mean radiative forcing values for Mt. Olympus plotted over one year for aged snow with three different d-BrC and BC concentrations— 10^2 ppb, 10^3 ppb and 10^4 ppb. The results for d-BrC are shown as bands between the two k_{550} values (0.1 and 0.25) representing the upper and lower bound of d-BrC absorption.

Fig. 4 | Spectral and broadband albedos of BC and d-BrC mixtures in aged snow. The spectral albedo in the visible and near-infrared (VNIR) wavelength region at a solar zenith angle (SZA) of 60° for the two 'base' BC concentrations (red lines) of (**a**) 10^2 ppb, and (**b**) 10^3 ppb. In both cases albedos corresponding to d-BrC:BC ratios of 4:1 (light brown lines) and 10:1 (dark brown lines) are considered. No LAP snow albedo (solid blue line) is included for reference. The pink (**a**) and green (**b**) shaded

areas show the range of experimental albedos measured using spectroradiometers by Kaspari et al.[17] at Mt. Olympus and Li et al.[53] in the Tibetan plateau, respectively. **c** shows the range of broadband albedos for the BC concentrations in (**a, b**) possible with literature reported d-BrC:BC ratios. Figure S10 shows the modeled spectral albedos for a 'base' BC concentration of 10 ppb.
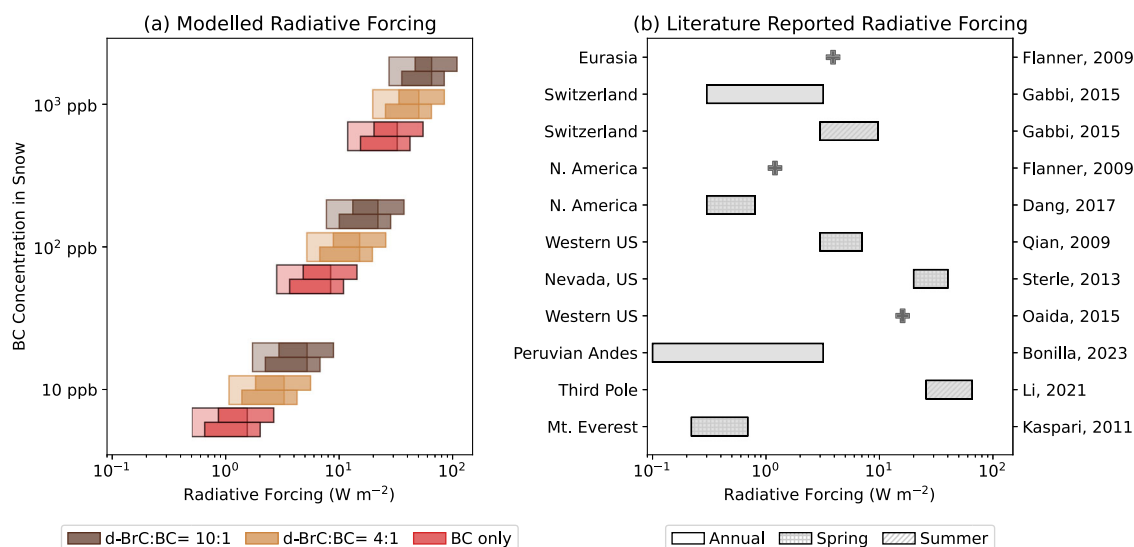
Fig. 5 | Radiative forcings of BC and d-BrC mixtures, and comparison with global literature values. a The annual-mean radiative forcing for simulated combinations of d-BrC and BC mixed in snow, grouped by 'base' concentrations of BC in snow of 10 ppb, 10^2 ppb, and 10^3 ppb. In each group, three concentration combinations of BC with d-BrC are identified: no d-BrC (red band), 4:1 d-BrC:BC (light brown band), and 10:1 d-BrC:BC (dark brown band). The horizontal length of each band represents the range of radiative forcing possible due to aerosol in fresh snow (left extremity of the band, 100 μm grain size) to aged snow (right extremity, 1000 μm grain size). A texture is given based on the averaging interval, whether seasonal (hatched) or annual (solid). **b** Globally reported ranges of seasonal and annual mean radiative forcing found in the literature[16,53,66–72].

coexisting in snow to determine the enhancement in RF compared to BC-only estimates. To do this, first we determined the spectral albedo for 9 combinations of interest: formed from a set of three BC concentrations (10, 10^2, and 10^3 ppb) and a set of three d-BrC:BC ratios (0, 4, and 10). The spectral albedos for the combinations involving BC 10 ppb are shown in Fig. S10, while the others are shown in Fig. 4 along with the corresponding broadband albedos.

With increasing BC concentration, there is a general decrease in spectral albedo (Fig. 4a, b). Moreover, for every order of magnitude increase in concentration until 10^3 ppb, this decrease grows larger. A similar trend is observed for d-BrC, where albedo perturbation from the baseline only-BC albedos rises with increasing concentration of d-BrC. Any d-BrC addition has the effect of further depressing the albedo at shorter wavelengths compared to other wavelengths, as expected from the spectral refractive index profile of d-BrC. Due to these factors, with increasing LAP concentration the spread of the albedo increases, so that for a base concentration of 10 ppb of BC the broadband albedo ranges from 0.88 to 0.90, for 10^2 ppb of BC it ranges from 0.78 to 0.86, and for 10^3 ppb of BC it ranges from 0.54 to 0.73 (Fig. 4c). The albedos simulated for mixtures with BC concentrations 10^2 ppb are largely consistent with the range of field-measured albedos from Kaspari et al.[17] who measured BC concentrations between 17 and 140 ppb, while for BC of concentration 10^3 ppb a reasonable match is seen with the field spectroscopy data from Li et al.[53] who measured BC concentrations between 1075 and 2027 ppb. From these spectral albedos, we then calculated the radiative forcing.

We note that the factors affecting the spectral albedo influence the radiative forcing in a similar fashion. An increase in LAP concentration in snow produces an increase in RF (Fig. 5a), just as it does with albedo perturbation. Addition of d-BrC at four times the abundance of BC leads to a radiative forcing enhancement from the BC-only baseline by 0.6–17.9 W m^{-2}, or by a factor of 1.6–2.1. From an annual mean RF of 1.57 W m^{-2} at a concentration of 10 ppb BC in aged snow, raising the BC concentration tenfold to 10^2 ppb BC yields an annual mean RF of 8.51 W m^{-2} (4.42 times increase), while an addition of 100 ppb d-BrC to the initial 10 ppb BC raises the RF to 5.28 W m^{-2} (2.36 times increase). The similar figures for fresh snow are 0.51 W m^{-2}, 2.86 W m^{-2} and 1.75 W m^{-2}. Thus, there is

considerable overlap between the range of RF for a mixture of BC and d-BrC with the concentration ratio d-BrC:BC = 10, and the range of RF for BC at a concentration an order of magnitude higher than that in the mixture (compare a dark brown band with the red band above it in Fig. 5a).

Seasonal mean RFs are also given for Northern Hemisphere spring (March–May) and summer (June–August). Snowmelt is higher within these seasons due to the relatively longer duration of solar incidence and smaller peak SZAs. At smaller SZAs, the albedo perturbation caused by a given aerosol-snow configuration is smaller than the same configuration at a larger SZA. It is therefore important to consider radiative forcing in spring and summer. The results show that for the Mt. Olympus site, the spring RF is consistently 30% higher and the summer RF is 70% higher than the corresponding annual mean RF. These results have implications for spring and summertime snow melt in midlatitude glaciers.

For situations involving both BC and d-BrC in snow together, it is important to note that RF is not additive, and therefore BC RF and d-BrC RF cannot be modeled separately and summed. For example, the annual mean RF due to a combination of 10^3 ppb BC and 10^4 ppb d-BrC (65.8 W m^{-2}) in aged snow is smaller than the sum of the RF due to 10^3 ppb BC alone (32.8 W m^{-2}) and 10^4 ppb d-BrC alone (59.9 W m^{-2}). This is due to the shadowing effect[53] where particles "shadow" one another by intercepting photons before other particles have a chance to absorb them. This reduces the amount of light available to additional particles for absorption thereby diminishing their albedo reduction capability. Thus, an incremental addition of LAP mass to dirty snow causes less RF than if that same mass concentration of LAP was mixed alone in clean snow. This is also evident from the fact that with the logarithmic increase in the concentration a commensurate logarithmic increase in RF is not observed. Instead, for a concentration increase of two orders of magnitude from 10 ppb to 10^3 ppb of BC in aged snow, the RF only increases from 1.58 W m^{-2} to 85.32 W m^{-2}, less than two orders of magnitude.

The modeled seasonal and annual mean RFs of this study are shown alongside literature RFs from around the world (Fig. 5b). The literature RFs include field observation-based RF calculations as well as forecasting model-based RF calculations. These 'real-world' RFs correspond to not only different geographic areas, but each study represents a unique parameter space,

including differing LAP species and their concentrations. There is considerable spread in these RF values, but also overlap with the modeled RFs of this study.

Discussion

Black carbon is the strongest absorbing aerosol species in the atmosphere and the dominant carbonaceous snow radiative forcing agent. But recent evidence from wildfires has shown the presence of strongly absorbing organic carbon particles, called dark-brown carbon (d-BrC) that exhibit stronger concentration-weighted absorption in comparison. These particles are insoluble in water and exhibit longer atmospheric absorption persistence. In this work, we study the sensitivity of snow albedo and radiative forcing due to d-BrC particles across a range of absorption strengths (imaginary refractive index) in combination with BC, at different time resolutions. While per particle, BC is a more powerful radiative forcer than any class of BrC, what d-BrC lacks in absorbing power is more than made up for by its higher abundance. The annual mean forcing due to concentration weighted d-BrC alone (four times the BC abundance) is at a minimum 22% greater than that due to BC alone. When this concentration-weighted d-BrC exists alongside BC, the resulting RF is 1.6 to 2.1 times the RF due to BC alone. This study improves snow radiative forcing estimates due to forest fires by accounting for d-BrC absorption, thereby making a more accurate assessment of biomass burning aerosols' impact on snow (Fig. 6). These results point to d-BrC as an important forcer whose snow radiative impact may be underestimated in regional and global models that can be used to improve the accuracy of radiative forcing estimates. Further, these results may be employed in establishing boundary conditions for weather and climate models.

The radiative forcings calculated in this study were for the specific midlatitude geographical coordinates corresponding to Mt. Olympus. Although there is spatial variability in surface albedos due to differing solar geometries and fluxes across geographies, these results may be extended to other mid latitude locations. Such variability in the mid latitudes is relatively small compared to polar latitudes, and the range of modeled RFs in the present study are in good agreement with those observed at multiple mid

latitude snowpack sites. It is important to note that these results are applicable to snow surfaces where wildfire aerosol deposition dominates. Elsewhere, other constituents may dominate light absorption, such as mineral dust[54], volcanic ash[9], and glacier algae[12]. Also, while LAP concentrations in snow are rarely uniform throughout a year and are prone to spike during wildfire season, this study establishes a framework for RF calculations which can be extended to situations including temporal variability in concentrations. However, the framework in its current form is not able to account for internal mixing, inclined snow surfaces, and the presence of cryoconite holes, which are important areas for future research. Further, other atmospheric aerosol constituents that are non-absorbing on their own, such as sulphates, may enhance absorption when present as a coating to BC or d-BrC. This is due to the well-documented lensing effect[55] and can cause further enhancement in radiative forcing, which would need to be accounted for.

This study has focused on the impact of mid-latitude wildfire emissions, particularly those containing d-BrC, on mid-latitude snowpack. Future work studying the effect of d-BrC on high-latitude snowpack and glaciers is planned. In such a study, instead of optically thick semi-infinite snow, a multilayered configuration of ice underlying snow that includes firn may be considered[56]. These efforts will help improve our understanding of the impact of LAPs on diverse snow and ice surfaces at a global scale.

The snow darkening effect has global climate implications. Snow surfaces with lowered reflectivity can raise the surface skin temperature by up to 6 K[57]. LAPs in snow are estimated to cause an effective radiative forcing in the atmosphere of $+0.08$ W m^{-2} (0.00 to $+0.18$ W m^{-2})[58]. These estimates however are from climate models that do not yet consider absorption by dark-brown carbon particles. Hence, the results from the present study highlight that the climate modeling radiative estimates are likely biased low. As the frequency of wildfires rises, accurately constraining the snow darkening effect due to all wildfire constituents will continue to grow in importance. The increased wildfires are likely to increase radiative forcing and snow melt, which has broad implications from the water security and the global climate perspectives. A recent study highlighting how mass loss from the Greenland Ice Sheet has been underestimated by up to 20% only underscores the pressing urgency of the glacier melt problem[59]. Results from the present study may lead to more accurately predicting glacier recession over long time horizons and help to manage the watersheds upon which water supply and agricultural irrigation depend on, including the Sierra Nevada, Andes, and Himalayas.

Methods
Aerosol optical properties
The brown-black absorption continuum parameterization described in Saleh et al.[29] was used to model the spectral imaginary refractive indices (k) over the range of d-BrC absorptivities considered. The parameterization is given by $k = \left(\frac{550}{\lambda}\right)^w k_{550}$, with the wavelength dependence $w = 7.6e^{-12.4k_{550}}$. Here, 550 nm is considered the reference wavelength, and hereafter, the imaginary refractive index (RI) at 550 nm, k_{550}, is used to distinguish between different shades of d-BrC.

The calculated spectral RIs are shown in Fig. S1 for d-BrC k_{550} between 0.1 and 0.25 at a resolution of 0.01. In contrast, the k_{550} for BrC in the default SNICAR[39,60] configuration is 0.03. For water-soluble BrC it is even lower, at 0.015 and 0.007 for BrC derived from fossil fuel combustion and biomass burning respectively[61]. The refractive indexes retrieved from real-world observed insoluble d-BrC particles sampled from wildfire emissions in the western U.S. were also considered[30] in addition to the brown-black continuum. As Fig. S1 shows, the wildfire emitted d-BrC RIs are within the range of d-BrC RIs modeled by the brown-black continuum. Additionally, BC in snow was simulated based on the refractive index parameterization given in Flanner et al.[39], which is based on the BC parameterization of Chang and Charalampopolous[52].

Visible and near-infrared wavelength interval of 400–1000 nm was chosen for the analysis. Above 1000 nm, the albedo reduction effect of LAPs in snow from a baseline scenario of no LAPs in snow is negligible because
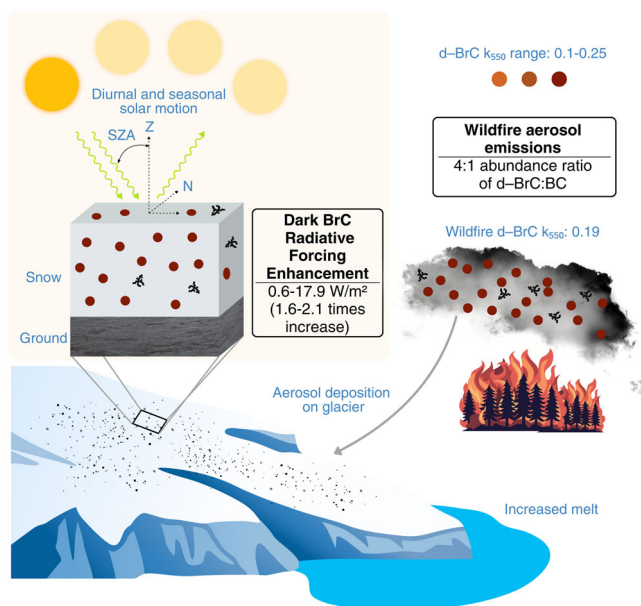

Fig. 6 | Schematic summarizing the main findings. The radiative forcing enhancement is the difference of the forcings between aged snow containing both wildfire d-BrC and BC, and aged snow containing just BC. The lower and upper ends of the range correspond to BC concentrations in snow of 10 ppb and 10^3 ppb respectively. The inset depicts a glacier cross-section showing the model configuration.
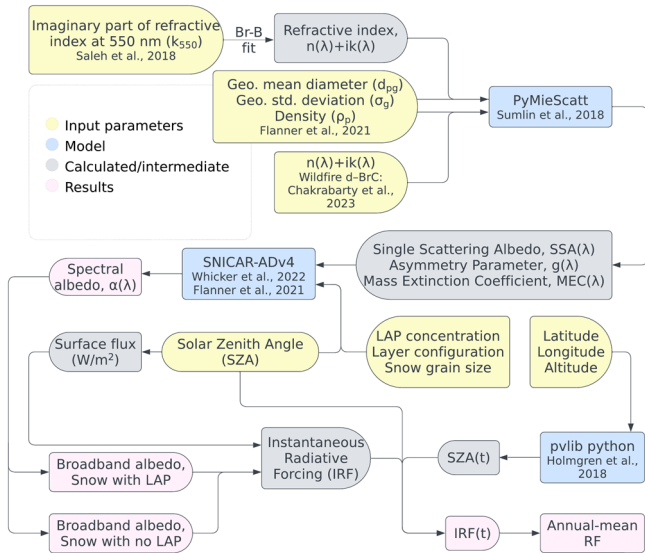
Fig. 7 | Flow chart of data flow throughout the analysis, beginning with the refractive indexes and size distribution of light-absorbing particles (LAPs). Other key inputs pertain to local environmental conditions and snow physical and microphysical properties. Key outputs include albedo and radiative forcing.

snow absorption dominates in the infrared regime[6]. Below 400 nm, the fraction of incident solar irradiance is relatively small (~7% of the flux).

Mie theory was then applied to the imaginary part of the refractive index data to calculate ensemble optical properties of the modeled and observed d-BrC tarballs: the single-scattering albedo (SSA), asymmetry parameter (g), and mass extinction cross-section (MEC). PyMieScatt, a Python-based package, was utilized for forward Mie calculations[62]. A log-normal size distribution with the default size distribution parameters from SNICAR were used for the calculations. The SSA was calculated as the ratio of the scattering β_{sca} and extinction coefficients β_{ext}:

$$SSA = \frac{\beta_{sca}}{\beta_{ext}} \qquad (2)$$

The mass extinction coefficient was found using the extinction efficiency Q_{ext} and the number size distribution n which are both functions of particle diameter d_p and the particle density ρ_p:

$$MEC = \frac{\int Q_{ext}(d_p)\frac{\pi d_p^2}{4}n\left(d_p\right)dd_p}{\rho_p \int \frac{\pi d_p^3}{6}n\left(d_p\right)dd_p} \qquad (3)$$

where the lognormal distribution is given by

$$n\left(d_p\right) = \frac{N}{\sqrt{2\pi}d_p\ln\left(\sigma_g\right)}\exp\left(-\frac{\left(\ln\left(d_p\right) - \ln\left(d_{pg}\right)\right)^2}{2\ln^2\left(\sigma_g\right)}\right) \qquad (4)$$

The numerator in Eq. (3) is equivalent to the calculated β_{ext}, while the integral in the denominator can be calculated as the numerical integration of the particle volume across the number size distribution.

For d-BrC k_{550} between 0.1 and 0.25 at a resolution of 0.01, forward Mie calculations were performed for wavelengths between 400 and 1000 nm at a resolution of 10 nm, for a lognormal size distribution with geometric median diameter $d_{pg} = 80 nm$ and geometric standard deviation $\sigma_g = 1.8$, and density $\rho_p = 1.27 g\ cm^{-3}$. Identical lognormal parameters were applied for BC, while for the wildfire-observed d-BrC, $d_{pg} = 170 nm$, $\sigma_g = 1.5$, and $\rho_p = 1.4 g\ cm^{-3}$. To verify our ensemble optical properties, we evaluated

the SSA, g and MEC calculated using PyMieScatt and the method described previously, against the optical properties calculated by Flanner et al.[39] for the above parameters and found a good match. The Mie theory-derived LAP optical properties (Fig. S2) were subsequently used as inputs to the SNICAR-based albedo simulations.

Modeling snow albedo
Simulations to determine spectral albedo were performed on the SNICAR model with Adding-Doubling solver, version 4 (SNICAR-ADv4)[39,40]. A sample simulation is shown in Fig. S3. In addition to the carbonaceous aerosol optical properties described above, the aerosol concentrations and snow microphysical properties (like the snow grain size) are key tunable variables. The aerosol particles are assumed to be distributed homogeneously and externally mixed with the snow grains for straightforward simulation. Although internal mixing is known to occur and causes enhanced absorption, there is large uncertainty in the nature and quantum of this mixing globally, with calculations estimating that between 32 and 73% of BC in surface snow is internally mixed[63].

A layer of optically thick snow – with no light reaching the underlying ground – is considered in SNICAR, which is representative of perennial mountainous snowpack that is being modeled. Optically thick snow is any snow with a depth greater than the penetration depth of broadband light (Fig. S4). Snow grain sizes were assumed to be 100 μm for fresh snow and 1000 μm for aged snow[39], and to be hexagonal plate shaped. Albedo results for snow containing grains intermediate in size lie between the fresh and aged snow albedo extremes. Therefore, only these two grain sizes were considered when accounting for snow age.

Simulations were performed for each LAP specie alone with no others present, and then for d-BrC and BC combinations. The spectral albedo from the SNICAR model is a function of wavelength, whereas the broadband albedo (Eq. 5) is a single measure weighted with respect to spectral irradiance:

$$\bar{\alpha} = \frac{\int_{400nm}^{1000nm}\alpha(\lambda)f(\lambda)d\lambda}{\int_{400nm}^{1000nm}f(\lambda)d\lambda} \qquad (5)$$

where $\alpha(\lambda)$ is spectral albedo and $f(\lambda)$ is the spectral fraction of the irradiance. Then, the broadband albedo reduction or perturbation from the clean snow albedo was calculated. The broadband albedo is a more useful measure of surface reflectivity than the spectral albedo, since it allows an easier comparison across cases and facilitates calculating the IRF. IRFs at 60° zenith angle for varying optical properties of d-BrC and snow age are shown in Fig. S6.

Modeling radiative forcing
Radiative forcing, both instantaneous and averaged over specific intervals of time, were then estimated from the albedos of snow with and without LAPs. IRF was calculated first from broadband albedos, which are a function of SZA, snow grain size, k_{550}, and the LAP concentration, according to Eq. 1. Note that the IRF varies with the time of the day since the albedo of a snow surface is unique to the solar position at a given instant. The solar position was calculated using the pvlib python package[64]. A library of lookup albedo values was developed to segmentalize the analysis into separate IRF and albedo calculations for computational efficiency. Supplementary Information sections 1 and 2 describe in further detail the dataflow and methodology of this analysis.

The mean of the IRF is determined over different timescales: annual, seasonal, and daily. The IRFs corresponding to all timestamps in a year at half-hour resolution are averaged to determine the surface annual-mean radiative forcing. For seasonal averages, Northern Hemisphere spring (March–May) and summer (June–August) are considered. For daily-mean RF, all IRF within 24-h time blocks beginning each day at midnight are individually averaged for every day in the year. A summary of the methods is shown in Fig. 7.

Data availability

The data obtained from this study are available upon request from the corresponding author (chakrabarty@wustl.edu).

Code availability

The SNICAR-ADv4 model used to perform snow-aerosol radiative transfer calculations is available at https://github.com/chloewhicker/SNICAR-ADv4. The computational package used to model optical properties of particles on the brown-black continuum is available at https://github.com/bsumlin/PyMieScatt. The computational package used to model the temporal variation of solar zenith angle is available at https://github.com/pvlib/pvlib-python.

References

1. Bond, T. C. et al. A technology-based global inventory of black and organic carbon emissions from combustion. *J. Geophys. Res. Atmospheres* **109**, 1–43 (2004).
2. Flanner, M. G., Zender, C. S., Randerson, J. T. & Rasch, P. J. Present-day climate forcing and response from black carbon in snow. *J. Geophys. Res. Atmos.* **112**, 1–17 (2007).
3. Hadley, O. L. & Kirchstetter, T. W. Black-carbon reduction of snow albedo. *Nat. Clim. Change* **2**, 437–440 (2012).
4. Skiles, S. M., Flanner, M., Cook, J. M., Dumont, M. & Painter, T. H. Radiative forcing by light-absorbing particles in snow. *Nat. Clim. Change* **8**, 964–971 (2018).
5. Wiscombe, W. J. & Warren, S. G. A model for the spectral albedo of Snow. I: pure snow. *J. Atmos. Sci.* **37**, 2712–2733 (1980).
6. Warren, S. G. & Wiscombe, W. J. A model for the spectral albedo of Snow. II: snow containing atmospheric aerosols. *J. Atmos. Sci.* **37**, 2734–2745 (1980).
7. Yu, Y. & Ginoux, P. Enhanced dust emission following large wildfires due to vegetation disturbance. *Nat. Geosci.* **15**, 878–884 (2022).
8. Gleason, K. E., Nolin, A. W. & Roth, T. R. Charred forests increase snowmelt: effects of burned woody debris and incoming solar radiation on snow ablation. *Geophys. Res. Lett.* **40**, 4654–4661 (2013).
9. Gelman Constantin, J. et al. Measurements and modeling of snow albedo at Alerce Glacier, Argentina: effects of volcanic ash, snow grain size, and cloudiness. *Cryosphere* **14**, 4581–4601 (2020).
10. Sarangi, C. et al. Dust dominates high-altitude snow darkening and melt over high-mountain Asia. *Nat. Clim. Change* **10**, 1045–1051 (2020).
11. Cook, J. M. et al. Glacier algae accelerate melt rates on the south-western Greenland Ice Sheet. *Cryosphere* **14**, 309–330 (2020).
12. Healy, S. M. & Khan, A. L. Albedo change from snow algae blooms can contribute substantially to snow melt in the North Cascades, USA. *Commun. Earth Environ.* **4**, 1–13 (2023).
13. Dennison, P. E., Brewer, S. C., Arnold, J. D. & Moritz, M. A. Large wildfire trends in the western United States, 1984–2011. *Geophys. Res. Lett.* **41**, 2928–2933 (2014).
14. Sicard, M. et al. Ground/space, passive/active remote sensing observations coupled with particle dispersion modelling to understand the inter-continental transport of wildfire smoke plumes. *Remote Sens. Environ.* **232**, 111294 (2019).
15. Aubry-Wake, C., Bertoncini, A. & Pomeroy, J. W. Fire and ice: the impact of wildfire-affected Albedo and irradiance on Glacier Melt. *Earths Future* **10**, e2022EF002685 (2022).
16. Bonilla, E. X. et al. Contribution of biomass burning to black carbon deposition on Andean glaciers: consequences for radiative forcing. *Environ. Res. Lett.* **18**, 024031 (2023).
17. Kaspari, S., McKenzie Skiles, S., Delaney, I., Dixon, D. & Painter, T. H. Accelerated glacier melt on Snow Dome, Mount Olympus, Washington, USA, due to deposition of black carbon and mineral dust from wildfire. *J. Geophys. Res. Atmos.* **120**, 2793–2807 (2015).
18. Lee, W.-L. et al. Impact of absorbing aerosol deposition on snow albedo reduction over the southern Tibetan plateau based on satellite observations. *Theor. Appl. Climatol.* **129**, 1373–1382 (2017).
19. Wang, Q. et al. Sources of carbonaceous aerosols and deposited black carbon in the Arctic in winter-spring: implications for radiative forcing. *Atmos. Chem. Phys.* **11**, 12453–12473 (2011).
20. Casey, K. A., Kaspari, S. D., Skiles, S. M., Kreutz, K. & Handley, M. J. The spectral and chemical measurement of pollutants on snow near South Pole Antarctica. *J. Geophys. Res. Atmos.* **122**, 6592–6610 (2017).
21. Usha, K. H., Nair, V. S. & Babu, S. S. Effects of aerosol–induced snow albedo feedback on the seasonal snowmelt over the Himalayan region. *Water Resour. Res.* **58**, e2021WR030140 (2022).
22. Senande-Rivera, M., Insua-Costa, D. & Miguez-Macho, G. Spatial and temporal expansion of global wildland fire activity in response to climate change. *Nat. Commun.* **13**, 1208 (2022).
23. Holden, Z. A. et al. Decreasing fire season precipitation increased recent western US forest wildfire activity. *Proc. Natl Acad. Sci.* **115**, E8349–E8357 (2018).
24. Lapuerta, M., González-Correa, S., Ballesteros, R., Cereceda-Balic, F. & Moosmüller, H. Albedo reduction for snow surfaces contaminated with soot aerosols: Comparison of experimental results and models. *Aerosol Sci. Technol.* **56**, 847–858 (2022).
25. Immerzeel, W. W. et al. Importance and vulnerability of the world's water towers. *Nature* **577**, 364–369 (2020).
26. Observations: Cryosphere. in *Climate Change 2013 – The Physical Science Basis* (ed. Intergovernmental Panel On Climate Change) 317–382 (Cambridge University Press, 2014). https://doi.org/10.1017/CBO9781107415324.012.
27. Bond, T. C. & Bergstrom, R. W. Light absorption by carbonaceous particles: an investigative review. *Aerosol Sci. Technol.* **40**, 27–67 (2006).
28. Yu, P. et al. Black carbon lofts wildfire smoke high into the stratosphere to form a persistent plume. *Science* **365**, 587–590 (2019).
29. Saleh, R., Cheng, Z. & Atwi, K. The brown–black continuum of light-absorbing combustion aerosols. *Environ. Sci. Technol. Lett.* **5**, 508–513 (2018).
30. Chakrabarty, R. K. et al. Shortwave absorption by wildfire smoke dominated by dark brown carbon. *Nat. Geosci.* **16**, 683–688 (2023).
31. Corbin, J. C. & Gysel-Beer, M. Detection of tar brown carbon with a single particle soot photometer (SP2). *Atmos. Chem. Phys.* **19**, 15673–15690 (2019).
32. He, C. Modelling light-absorbing particle–snow–radiation interactions and impacts on snow albedo: fundamentals, recent advances and future directions. *Environ. Chem.* **19**, 296–311 (2022).
33. Liu, D., He, C., Schwarz, J. P. & Wang, X. Lifecycle of light-absorbing carbonaceous aerosols in the atmosphere. *Npj Clim. Atmos. Sci.* **3**, 1–18 (2020).
34. Zhou, Y. et al. Measurement report: molecular composition, optical properties, and radiative effects of water-soluble organic carbon in snowpack samples from northern Xinjiang, China. *Atmos. Chem. Phys.* **21**, 8531–8555 (2021).
35. Li, C. et al. Sources of black carbon to the Himalayan–Tibetan Plateau glaciers. *Nat. Commun.* **7**, 12574 (2016).
36. Hagler, G. S. W. et al. Particulate and water-soluble carbon measured in recent snow at Summit, Greenland. *Geophys. Res. Lett* **34**, 1–5 (2007).
37. Doherty, S. J. et al. Observed vertical redistribution of black carbon and other insoluble light-absorbing particles in melting snow. *J. Geophys. Res. Atmos.* **118**, 5553–5569 (2013).
38. Beres, N. D., Sengupta, D., Samburova, V., Khlystov, A. Y. & Moosmüller, H. Deposition of brown carbon onto snow: changes in

snow optical and radiative properties. *Atmos. Chem. Phys.* **20**, 6095–6114 (2020).

39. Flanner, M. G. et al. SNICAR-ADv3: a community tool for modeling spectral snow albedo. *Geosci. Model Dev.* **14**, 7673–7704 (2021).

40. Whicker, C. A. et al. SNICAR-ADv4: a physically based radiative transfer model to represent the spectral albedo of glacier ice. *Cryosphere* **16**, 1197–1220 (2022).

41. Beres, N. D., Lapuerta, M., Cereceda-Balic, F. & Moosmüller, H. Snow surface albedo sensitivity to black carbon: radiative transfer modelling. *Atmosphere* **11**, 1077 (2020).

42. Wang, X., Shi, T., Zhang, X. & Chen, Y. An overview of snow albedo sensitivity to black carbon contamination and snow grain properties based on experimental datasets across the Northern Hemisphere. *Curr. Pollut. Rep*. **6**, 368–379 (2020).

43. Kang, S., Zhang, Y., Qian, Y. & Wang, H. A review of black carbon in snow and ice and its impact on the cryosphere. *Earth Sci. Rev.* **210**, 103346 (2020).

44. Lim, S. et al. Black carbon variability since preindustrial times in the eastern part of Europe reconstructed from Mt. Elbrus, Caucasus, ice cores. *Atmos. Chem. Phys.* **17**, 3489–3505 (2017).

45. Osmont, D. et al. An 800-year high-resolution black carbon ice core record from Lomonosovfonna, Svalbard. *Atmos. Chem. Phys.* **18**, 12777–12795 (2018).

46. Réveillet, M. et al. Black carbon and dust alter the response of mountain snow cover under climate change. *Nat. Commun.* **13**, 5279 (2022).

47. Lin, G. et al. Radiative forcing of organic aerosol in the atmosphere and on snow: effects of SOA and brown carbon. *J. Geophys. Res. Atmos.* **119**, 7453–7476 (2014).

48. Warren, S. G. Optical properties of snow. *Rev. Geophys.* **20**, 67–89 (1982).

49. Marsh, P. Grain growth in a wet arctic snow cover. *Cold Reg. Sci. Technol.* **14**, 23–31 (1987).

50. Warren, S. G. Optical properties of ice and snow. *Philos. Trans. R. Soc. Math. Phys. Eng. Sci.* **377**, 20180161 (2019).

51. Miller, S. D. et al. Satellite-based estimation of temporally resolved dust radiative forcing in snow cover. *J. Hydrometeorol.* **17**, 1999–2011 (2016).

52. Chang, H. & Charalampopoulos, T. T. Determination of the wavelength dependence of refractive indices of flame soot. *Proc. Math. Phys. Sci.* **430**, 577–591 (1990).

53. Li, Y. et al. Black carbon and dust in the Third Pole glaciers: revaluated concentrations, mass absorption cross-sections and contributions to glacier ablation. *Sci. Total Environ.* **789**, 147746 (2021).

54. Skiles, S. M. & Painter, T. H. Assessment of radiative forcing by light-absorbing particles in snow from in situ observations with radiative transfer modeling. *J. Hydrometeorol.* **19**, 1397–1409 (2018).

55. Pu, W. et al. Enhancement of snow albedo reduction and radiative forcing due to coated black carbon in snow. *Cryosphere* **15**, 2255–2272 (2021).

56. Amory, C. et al. Firn on ice sheets. *Nat. Rev. Earth Environ.* **5**, 79–99 (2024).

57. Yasunari, T. J., Koster, R. D., Lau, W. K. M. & Kim, K.-M. Impact of snow darkening via dust, black carbon, and organic carbon on boreal spring climate in the Earth system. *J. Geophys. Res. Atmos.* **120**, 5485–5503 (2015).

58. The Earth's Energy Budget, Climate Feedbacks and Climate Sensitivity. in *Climate Change 2021 – The Physical Science Basis: Working Group I Contribution to the Sixth Assessment Report of the Intergovernmental Panel on Climate Change* (ed. Intergovernmental Panel on Climate Change (IPCC)) 923–1054 (Cambridge University Press, Cambridge, 2023). https://doi.org/10.1017/9781009157896.009.

59. Greene, C. A., Gardner, A. S., Wood, M. & Cuzzone, J. K. Ubiquitous acceleration in Greenland Ice Sheet calving from 1985 to 2022. *Nature* **625**, 523–528 (2024).

60. Kirchstetter, T. W., Novakov, T. & Hobbs, P. V. Evidence that the spectral dependence of light absorption by aerosols is affected by organic carbon. *J. Geophys. Res. Atmos.* **109**, 1–12 (2004).

61. Yue, S. et al. Brown carbon from biomass burning imposes strong circum-Arctic warming. *One Earth* **5**, 293–304 (2022).

62. Sumlin, B. J., Heinson, W. R. & Chakrabarty, R. K. Retrieving the aerosol complex refractive index using PyMieScatt: a Mie computational package with visualization capabilities. *J. Quant. Spectrosc. Radiat. Transf.* **205**, 127–134 (2018).

63. Flanner, M. G., Liu, X., Zhou, C., Penner, J. E. & Jiao, C. Enhanced solar energy absorption by internally-mixed black carbon in snow grains. *Atmos. Chem. Phys.* **12**, 4699–4721 (2012).

64. Holmgren, W. F., Hansen, C. W. & Mikofski, M. A. pvlib python: a python package for modeling solar energy systems. *J. Open Sour. Softw.* **3**, 884 (2018).

65. Saleh, R. From measurements to models: toward accurate representation of brown carbon in climate calculations. *Curr. Pollut. Rep.* **6**, 90–104 (2020).

66. Dang, C. et al. Measurements of light-absorbing particles in snow across the Arctic, North America, and China: effects on surface albedo. *J. Geophys. Res. Atmos.* **122**, 10,149–10,168 (2017).

67. Flanner, M. G. et al. Springtime warming and reduced snow cover from carbonaceous particles. *Atmos. Chem. Phys.* **9**, 2481–2497 (2009).

68. Gabbi, J., Huss, M., Bauder, A., Cao, F. & Schwikowski, M. The impact of Saharan dust and black carbon on albedo and long-term mass balance of an Alpine glacier. *Cryosphere* **9**, 1385–1400 (2015).

69. Kaspari, S. D. et al. Recent increase in black carbon concentrations from a Mt. Everest ice core spanning 1860-2000 AD. *Geophys. Res. Lett.* **38**, 1–6 (2011).

70. Oaida, C. M. et al. Improving snow albedo processes in WRF/SSiB regional climate model to assess impact of dust and black carbon in snow on surface energy balance and hydrology over western U.S. *J. Geophys. Res. Atmos.* **120**, 3228–3248 (2015).

71. Qian, Y., Gustafson, W.I., Leung, L. R. & Ghan, S. J. Effects of soot-induced snow albedo change on snowpack and hydrological cycle in western United States based on Weather Research and Forecasting chemistry and regional climate simulations. *J. Geophys. Res. Atmos.* **114**, 1–19 (2009).

72. Sterle, K. M., McConnell, J. R., Dozier, J., Edwards, R. & Flanner, M. G. Retention and radiative forcing of black carbon in eastern Sierra Nevada snow. *Cryosphere* **7**, 365–374 (2013).

Acknowledgements

Author contributions

G.S.C. and R.K.C. conceptualized the study. G.S.C. designed and carried out the modeling experiments, with help from T.S.K. G.S.C. wrote the manuscript with input from T.S.K. and R.K.C. G.S.C. and T.S.K. created the figures. R.K.C. was responsible for funding acquisition. All authors contributed to the scientific discussion and interpretation of the results as well as to the final manuscript review and editing.

Competing interests

The authors declare no competing interests.

Additional information